Microscopic Topography of Heterocrystal Interfaces

Brian Olmsted, Sylvie Ferlay, Pierre Dechambenoit, Mir Wais Hosseini, Michael Ward

Microscopic Topography of Heterocrystal Interfaces

*Brian K. Olmsted,[†] Sylvie Ferlay,[§] Pierre Dechambenoit,[§] Mir Wais Hosseini[§] and Michael D. Ward[†,]**

Contribution from the Department of Chemistry and the Molecular Design Institute, New York University, 100 Washington Square East, New York, NY 10003-6688,USA, and the Laboratoire de Coordination Organique, UMR CNRS 7140, Université de Strasbourg, 4, rue Blaise Pascal, 67008 Strasbourg, France

Received Date:_____; Email: mdw3@nyu.edu

Abstract

Real-time *in situ* atomic force microscopy (AFM) of the (010) and (001) planes of isomorphous [1,4-bis(amidinium)benzene]$_2$M(CN)$_6$·8H$_2$O (M = Fe, Ru) crystals, known to exhibit growth of one of the metallate compounds on the other to produce "core-shroud" heterocrystals, reveals high-fidelity epitaxial growth during heterocrystal formation or roughened surfaces, depending on the crystal face and crystallization conditions. The roughened crystal surfaces that define the interface between heteroepitaxial layers under typical growth conditions are consistent with the interface structure observed by electron dispersive spectrometry, which indicated intermixing of the two materials throughout a 0.7 μm-thick interfacial region, but could not distinguish between various possible mechanisms for the intermixing. The crystal topography and roughness under various conditions reveal that the intermixing zone observed during heterocrystal formation may be a consequence of a rough growth surface on the inner "core" crystal upon evaporation of solvent prior to immersion in the growth medium used for epitaxial crystallization of the second compound. These observations suggest that the roughness of the growth interface can be regulated using specific growth protocols that minimize the intermixing of the two compounds.

Keywords: Atomic force microscopy, crystal growth, epitaxy, heteroepitaxy

[†]New York University

[§]Université de Strasbourg

*To whom correspondence should be addressed

Submitted to *Crystal Growth & Design* February 3, 2009

Table of Contents Graphic and Summary

Brian K. Olmsted, Silvie Ferlay, Pierre Dechambenoit, M. Wais Hosseini and Michael D. Ward

Crystal Growth & Design, **2009**, *00*, 0000.

Microscopic Topography of Heterocrystal Interfaces

Summary

Atomic force microscopy (AFM) of the prominent surfaces of isomorphous [1,4-bis(amidinium)benzene]$_2$-M(CN)$_6$·8H$_2$O (M = Fe, Ru) crystals, known to exhibit growth of one of the metallate compounds on the other to produce "core-shroud" heterocrystals, reveals high-fidelity epitaxial growth or roughened surfaces, depending on the crystal face and crystallization conditions. The rough crystal surfaces are consistent with the metallate intermixing zone observed for heterocrystals prepared under typical conditions wherein the inner core crystal surface roughens considerably upon evaporation of solvent prior to immersion in the growth medium containing the shroud compound.

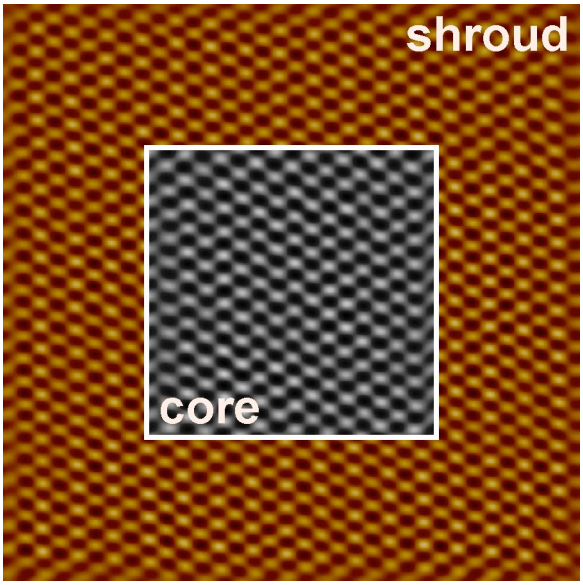

Introduction

Heteroepitaxial growth of single crystals on single crystal substrates is well established for inorganic materials and has become a mainstay of the electronics industry.[1,2,3,4,5] The epitaxial growth of organic crystals on organic crystal substrates, although less well developed compared with inorganic materials, has emerged as an active subject of research owing to its impact on technology, ranging from new electronic materials to pharmaceuticals. [6,7,8,9] These investigations have included the use of single crystal substrates for controlling nucleation and polymorphism,[10] the growth of heteroepitaxial organic thin films relevant to electronic applications,[11] and elucidation of epitaxy mechanisms,[12] which can be more complex than those of their inorganic counterparts owing to weaker intermolecular bonding and lower crystal symmetry.[13] Epitaxy concepts have been invoked to explain the formation of molecular crystal composites, in which compounds with nearly identical crystal structures but different compositions form "heterocrystals" in which one compound surrounds the other.[14,15,16] One rather comprehensive study has demonstrated that epitaxial growth between phases of isostructural metal complexes occurs more readily for interfaces defined by smaller strain and comparable surface structure. Recently this has been demonstrated for nanoparticles based on coordination networks.[17] When combined with the versatility of molecular design and organic synthesis, the ability to fabricate such "heterocrystal" composites significantly broadens the range of available materials.

Recently, one of our laboratories reported the syntheses of mm-scale "crystals of crystals," heterocrystals in which a single crystal of a complex molecular salt (denoted here as a "core"), assembled through charge-assisted hydrogen bonding, was completely encapsulated by an isomorphous crystalline phase (denoted here as a "shroud") that differed from the core crystal with respect to an interchangeable hexacyanometallate anion.[18] Single crystal diffraction of these composite crystals, composed of $(C_{14}N_4H_{20})_2^{2+}(Fe^{II}(CN)_6)^{4-}\cdot 8H_2O$ (**1-Fe**) and $(C_{14}N_4H_{20})_2^{2+}(Ru^{II}(CN)_6)^{4-}\cdot 8H_2O]$ (**1-Ru**) (Scheme 1) revealed that single crystallinity was preserved throughout the composite crystal, suggesting epitaxial alignment of each set of isomorphous crystal faces.[19] The crystal faces are characterized by hydrogen-bonding networks propagating along vectors that define the crystal plane, with water molecules of the octamers bridging cyanometallate anions along the [100] direction through O-H…$^{-}$NC hydrogen bonds, charge-assisted $^{+}$N-H…$^{-}$NC hydrogen bonding between the bis(amidinium) cations and the cyanometallate anions along the [010] direction, and hydrogen-bonded water bridges along [001] (Figure 1).

Transmission electron microscopy (TEM) and electron dispersive spectrometry (EDS) revealed that the interface between the two isomorphous compounds in a core-shroud composite crystal was characterized by a zone of intermixed $Fe(CN)_6^{4-}$ and $Ru(CN)_6^{4-}$ with a thickness of 0.7 μm (Figure 2).[20] TEM, however, could not discriminate between different mechanisms for this intermixing, which may result from roughening of the core crystals prior to or during epitaxial growth of the second compound as a

consequence of dissolution and growth cycles, crystal aggregates of the core crystal that deposit non-uniformly on its surface, or solid state interdiffusion of the two anions, although this would be expected to be slow.

We describe herein the characterization of the epitaxial growth surfaces responsible for formation of the **1-Fe**/**1-Ru** core-shroud heterocrystals by *in situ* atomic force microscopy (AFM), a method that has proven useful in probing the surfaces of various molecular crystals during *in situ* growth.[21] The large (010) and (001) faces exhibit well-defined terraces with step heights corresponding to a single unit cell (d_{010} and d_{001}, respectively). Lattice images for the (001) face of each compound, acquired in saturated solutions, reveal surface lattice parameters reflecting those expected from single crystal structure analysis. Furthermore, the observation of these lattice images signifies extraordinary order, structural integrity and molecular flatness for this crystal plane. These characteristics enable the observation of epitaxial growth of a "shroud" phase on the (001) surface of the isostructural "core" crystal, with perfect alignment of the crystal lattices. In contrast, the (010) surface exhibits continuous dissolution and regrowth, which precludes the formation of a smooth growth interface. The topography of crystal surfaces generated under conditions used to form the composite crystals suggests that the source of the composition intermixing zone at the crystal-crystal interface is the deposition of crystalline core material from highly supersaturated solutions present during evaporation of solvent from the crystal surfaces prior to immersion in the solution containing the second isomorphous compound. These studies add to the understanding of the structure of interfacial regions in molecular heterocrystals, which may be vital for advances in complex materials that may be used in optics, optoelectronics, and photorefractive applications that rely on the difference in the refractive index of the isostructural layers.[22,23,24]

Scheme 1

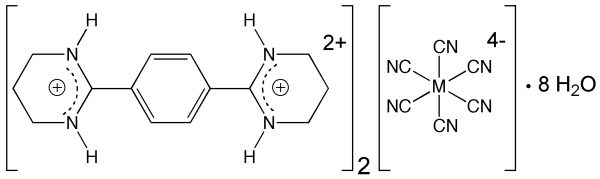

1-Fe (M = Fe)
1-Ru (M = Ru)

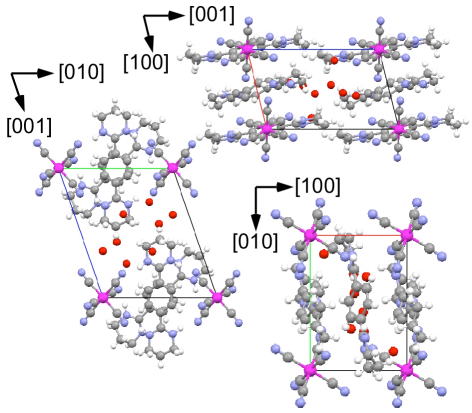

Figure 1. Molecular packing of the bis(amidinium) cations and the cyanometallate anions viewed along the *a*-axis (left), the *b*-axis (upper-right), and the *c*-axis (lower-right). The positions of the eight water molecules are denoted by their oxygen atoms (red).

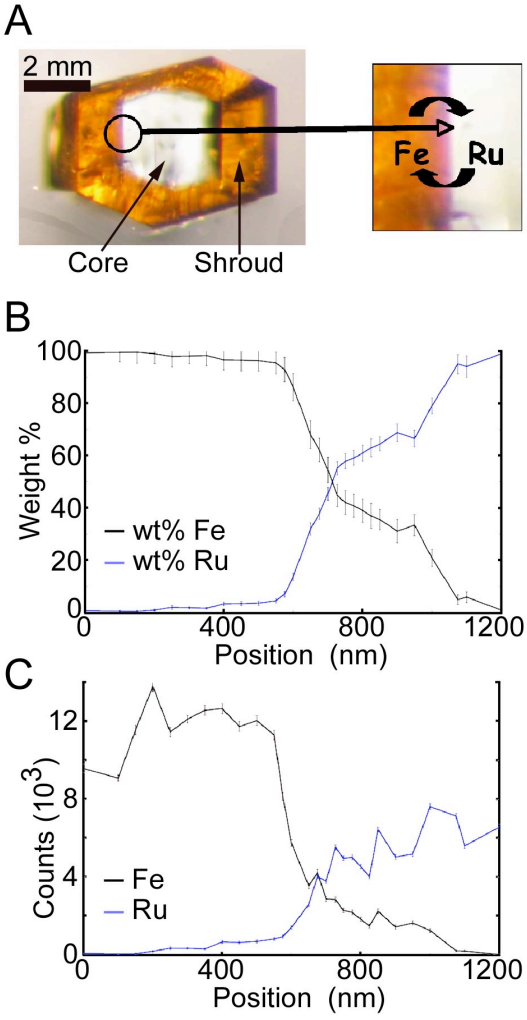

Figure 2. (A) Heterocrystal formed through epitaxial growth of a shroud of **1-Fe** (orange) on a core seed crystal of **1-Ru** (colorless). (B,C) Energy dispersive spectroscopy profiles of the Fe and Ru content across the heterocrystal interface, expressed as count rate for Fe–K and Ru–L signals and weight percent (reproduced with permission from Reference 20).

Results and Discussion

Compounds **1-Fe** and **1-Ru** are isomorphous, with nearly identical lattice parameters and identical molecular packing (Table 1).[19] A 50:50 solid solution grown from aqueous solutions containing a mixture of **1-Fe** and **1-Ru** afforded crystalline solid solutions with lattice parameters intermediate to those of the two individual compounds as expected for Vegard's law.[25] This behavior, not unlike that observed for other molecular crystal alloys,[26] corroborates the isomorphous nature of **1-Fe** and **1-Ru**. In order to explore the epitaxial growth surfaces involved in heterocrystal formation, crystals of **1-Fe** and **1-Ru** were grown separately from aqueous solutions containing 0.02M $[(C_{14}N_4H_{20})_2][\text{tosylate}]_2$ and 0.01M $K_4M(CN)_6$ (M = Fe or Ru) over a period of two days at room temperature. The crystals were harvested and carefully dried under a gentle nitrogen stream. The crystals exhibited a rectangular habit, with one axis much longer than the others (Figure 3). X-ray diffraction (and subsequently, AFM) revealed that the long axis of the crystal coincided with the [100] direction, with large (010) and (001) faces assignable to the sides of the rectangular crystals.

Table 1. Crystallographic parameters for $[C_{14}N_4H_{20}^{2+}]_2[Fe(CN)_6^{4-})]\cdot 8H_2O$ (**1-Fe**) and $[C_{14}N_4H_{20}^{2+}]_2[Ru(CN)_6^{4-})]\cdot 8H_2O$ (**1-Ru**), measured at 173 K (see reference 25)

	1-Fe	**1-Ru**
Space group	*P*-1	*P*-1
a (Å)	7.6538(2)	7.6658(2)
b (Å)	10.9276(3)	10.9443(3)
c (Å)	13.4639(3)	13.4958(4)
α (deg))	70.260(5)	70.252(2)
β (deg)	75.085(5)	75.065(2)
γ (deg)	85.502(5)	85.455(2)
Volume ($Å^3$)	1024.16	1029.63(5)

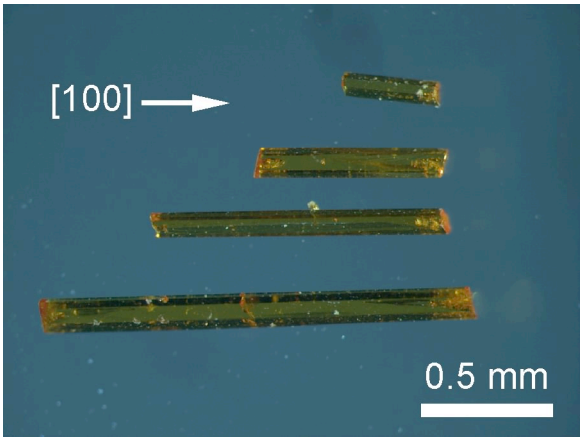

Figure 3. Illustrative **1-Fe** crystals used for AFM studies. The direction of the long-axis was verified as [100] by single crystal X-Ray diffraction and AFM. The dominant faces traversing the long axis of the crystal were assignable to (010) and (001). Other faces with less morphological importance were assignable to (011) and (023).

Growth of 1-Fe and 1-Ru single crystals. Crystals of **1-Fe** and **1-Ru** prepared in the manner described above were mounted to separate AFM sample stages with a UV-curable epoxy that was inert to aqueous media. Initially, AFM images acquired in air for the larger faces revealed finger-like features aligned with the [100] direction with a maximum feature height of approximately 200 nm above the basal surface (Figure 4). Because the crystals were removed directly from the growth solution and dried with nitrogen, highly supersaturated conditions were expected during the final stages of drying. This condition would be expected to result in rapid crystal growth, which is consistent with the roughened interface and finger-like features.[27,28] These features disappeared within five minutes of immersion in deionized water while collecting images in the AFM cell, as expected for surface features with high radii of curvature,[29,30,31,32] followed by a slower dissolution that produced large flat regions (Figure 4). These flat regions contained long fissures aligned with the [100] direction. The crystal surface changed substantially during the acquisition timescale for consecutive images (*ca.* 20 seconds acquisition time per image), which complicated definitive assignment of dissolution rates for specific crystal faces. Replacement of the deionized water with a 0.005 M aqueous solution of either **1-Fe** (to mounted **1-Fe** crystals) or **1-Ru** (to mounted **1-Ru** crystals) in the AFM cell, with the crystal in contact with the liquid media throughout, reduced the etching rate to negligible amounts while repairing the [100] fissures and producing a flattened topography decorated with well-defined terraces (Figure 5). The heights of the steps separating the terraces were either 10.55 Å or 12.49 Å, corresponding to d_{010} = 10.300 Å and d_{001} = 12.311 Å. These values confirm that the crystal faces in each image are (010) and (001), both which contain the [100] direction and support the assignment of the [100] direction to the long axis of the crystal.

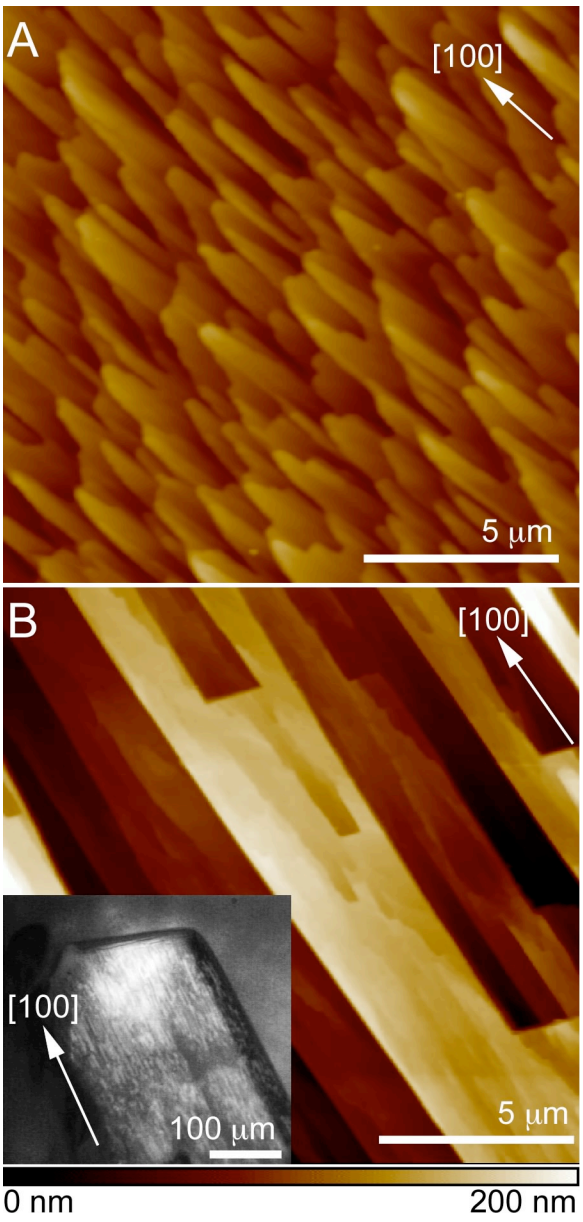

Figure 4. (A) An image acquired using contact mode with constant cantilever deflection (*i.e.* height image) of one of the dominant crystal faces traversing the [001] axis in **1-Ru** (in air). The image was acquired after the crystal was harvested from the growth medium and dried in a gentle nitrogen stream. The finger-like features coincide with the [100] direction of the crystal. The root-mean-square roughness is 14.5 nm. (B) An image acquired in deionized water using contact mode with constant cantilever deflection (*i.e.* height image) for **1-Fe** after immersion in deionized water for 20 minutes. The root-mean-square roughness is 67 nm. (inset) Optical micrograph of a crystal of **1-Fe**. Fissures aligned with the [100] direction appeared on the exposed surfaces of the crystal after it was immersed in deionized water for 20 minutes.

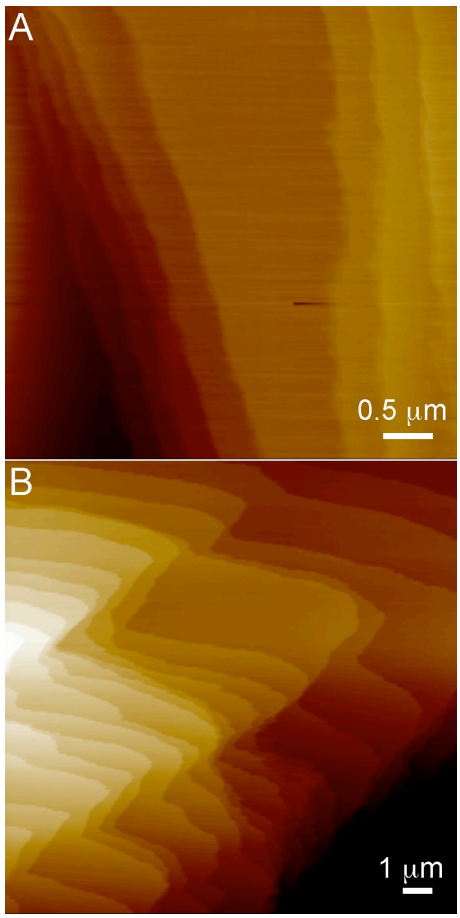

Figure 5. (A) AFM image acquired for the (010) face of a single crystal of **1-Ru** in 0.005 M **1-Ru** using contact mode while scanning at constant deflection (*i.e.* height mode), revealing well-defined terraces. The measured step heights averaged 10.55 Å, corresponding to d_{010} (10.300 Å). (B) AFM image acquired for the (001) face of a single crystal of **1-Ru** in 0.005 M **1-Ru** using contact mode while scanning at constant deflection (*i.e.* height mode). The measured step heights averaged 12.49 Å, corresponding to d_{001} (12.311 Å).

Epitaxial Growth. Lattice images of crystalline surfaces can be captured if the region beneath the tip is flat, on the molecular level, over an area that is large compared with the radius of curvature of an AFM tip (20-60 nm). Acquisition of a lattice image is best achieved if dissolution or growth on the crystal surface is slow compared with the time scale required for capture of a complete image. Acquisition of lattice images of **1-Fe** and **1-Ru** in aqueous media was usually difficult due to rapid dissolution or growth when immersed in slightly undersaturated or slightly oversaturated growth solutions, respectively. Nonetheless, lattice images of the (001) face of **1-Ru** and **1-Fe** (Figure 6) could be acquired by judiciously maintaining the solution concentration at saturation. The 2D lattice parameters determined from AFM lattice images of the (001) faces for both the **1-Ru** and **1-Fe** crystals corroborate the assignment above discerned from step height data. The lattice parameters are somewhat larger than those expected from the single crystal structures of **1-Ru** and **1-Fe**. This apparent discrepancy can be attributed to experimental error (typically

5%) and thermal expansion, given that the temperature of the AFM data acquisition (298 K) was higher than the X-ray data collection temperature (173 K).

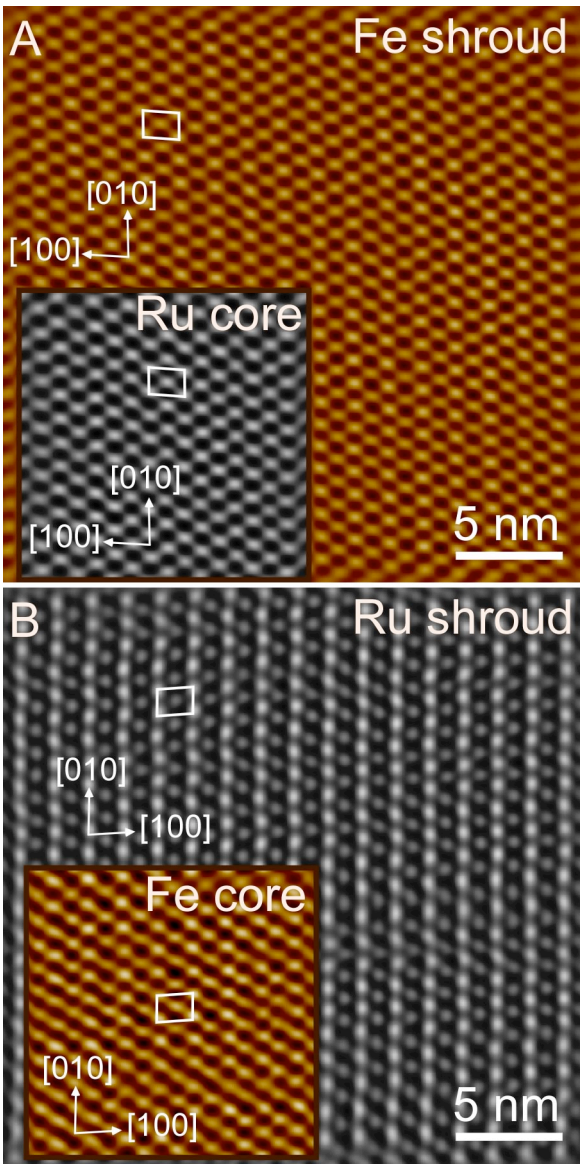

Figure 6. Composite lattice images, after Fourier transformation, for the (001) face of a core crystal (insets) and the epitaxially aligned (001) face of the shroud overlayer: (A) **1-Fe** overlayer grown on the (001) face of a **1-Ru** crystal; (B) **1-Ru** overlayer grown on the (001) face of a **1-Fe** crystal. Both cases display an extraordinary degree of epitaxial alignment between the core and the shroud. The lattice parameters deduced from the images correspond to those expected for the (001) plane of **1-Fe** and **1-Ru** (**1-Fe**: *a* = 7.68 Å, *b* = 11.23 Å, γ = 85.5°; **1-Ru**; *a* = 8.00 Å; *b* = 11.62 Å, γ = 85.5°). From crystal structures: **1-Fe**: *a* = 7.6538 Å, *b* = 10.9276 Å, γ = 85.502°; **1- Ru**: *a* = 7.6658 Å, *b* = 10.9443 Å, γ = 85.455°. The corresponding raw data images are provided in Supporting Information.

Notably, lattice images of the (001) face also were observed for **1-Fe** overlayers grown on **1-Ru** crystals, and vice versa, from a super-saturated solution of the corresponding overlayer compound (Figure

6). In each case, the lattice orientation of the overlayer, which corresponds to the shroud, is identical to the core crystal, confirming the presence of an epitaxial relationship governing the growth of a shroud around the core. Numerous attempts to capture lattice images of the (010) faces of **1-Fe** and **1-Ru** on the time scale of image acquisition (1-5 seconds per frame), however, were unsuccessful due to an apparent dynamic dissolution and re-growth (see below).

Interface width and crystal growth conditions. The topographies of the flat (010) and (001) faces of **1-Fe** and **1-Ru** changed substantially upon drying the crystals in the AFM cell. When crystals immersed in saturated solutions were rinsed with deionized water and then dried under nitrogen, randomly oriented pyramidal islands with well-defined facets appeared on both faces, with heights ranging from 20 nm to 1 μm (Figure 7A). These features are presumed to be a consequence of rapid deposition during drying of **1-Fe** or **1-Ru** that had dissolved when contacted with water. Notably, removal of the saturated solution without a deionized water rinse produced well-defined rectangular features resembling the bulk crystal habit (Figure 7B). These features were aligned with the [100] direction of the underlying surface, similar to the finger-like features in Figure 4A. The root-mean-square roughness of this surface (54 nm) was much less than that observed after drying from deionized water (177 nm). The maximum height of these features was 200 nm, comparable with the maximum height of the finger-like features in Figure 4A. These observations argue that contact with deionized water results in dissolution at the surface, creating defects that spawn the growth of spurious misoriented crystals. In contrast, drying directly from a saturated solution would be expected to prevent dissolution at the crystal surface, thus preserving the integrity of the flat regions that would support epitaxial growth and the formation of the aligned rectangular features.

It is reasonable to suggest that the roughness adopted by the **1-Fe** and **1-Ru** crystal surfaces under either condition may be responsible for the 700 nm-thick intermixing zone observed by EDS, particularly core crystals that are rinsed with pure water prior to drying and subsequent immersion in a solution of the shroud compound, as schematically represented in Figure 8. These observations also argue that the thickness of the intermixing zone would be minimized by prolonged exposure of the crystal surface to a saturated solution (*i.e.* not undersaturated or supersaturated) to form an ultraflat surface, followed by replacement of the liquid medium, without drying, by a slightly supersaturated solution of the other cyanometallate compound. This treatment would be conducive to epitaxial growth on a smooth interface, as evidenced by the images in Figures 5 and 6, and a more distinct boundary between the core and shroud. Furthermore, the core surface would not dissolve and redeposit under these conditions, thus preserving the distinct boundary regardless of the roughness of the overlayer phase. We also note that crystal growth on a flat basal plane of the same material at a relative supersaturation of $s > 2$ produced oriented features

as tall as 800 nm (Figure 9), suggesting that growth of the core crystal under such conditions can lead to an intermixing zone with a thickness comparable to that measured by EDS.

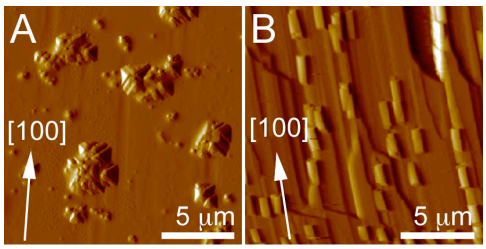

Figure 7. (A) AFM image acquired in air, using contact mode while scanning at constant height (*i.e.*, deflection mode), for a single crystal of **1-Ru** after it was rinsed with deionized water for five minutes and dried under a gentle nitrogen stream. (B) AFM image acquired in air for a single crystal of **1-Ru** after immersion in saturated **1-Ru** (roughly 0.005 M) for five minutes followed by drying under a gentle nitrogen stream, without rinsing with deionized water. The aligned rectangular features on the surface resemble the bulk growth habit for these crystals.

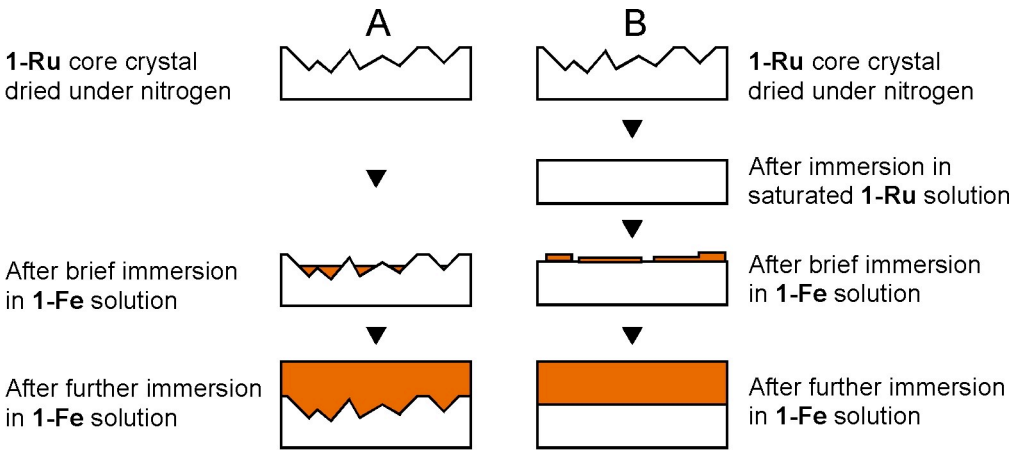

Figure 8. (A) Evolution of a core-shroud (white-orange, as in the example depicted in Figure 2A) heterocrystal under conditions favoring prior formation of a roughened core crystal surface, leading to a thick intermixing zone. (B) Evolution of the same core-shroud heterocrystal under conditions favoring formation of a distinct interface between the two isomorphous compounds, producing a minimal intermixing zone.

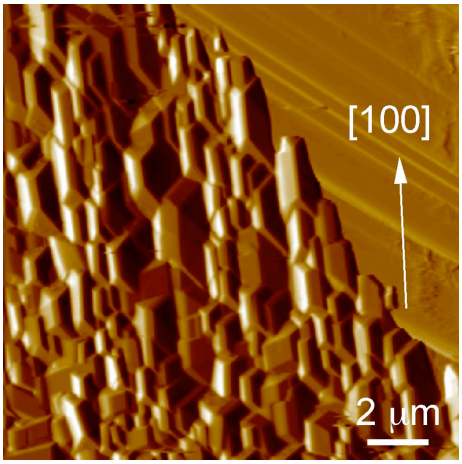

Figure 9. *In situ* AFM image acquired using contact mode while scanning at constant height (*i.e.*, deflection mode) during growth of **1-Ru** on a crystal of **1-Ru** that was first treated to produce a flat surface. The terraces on the basal plane, visible in the upper right corner, are defined by steps along the [110] direction.

Relationship between crystal structure and roughening. The difficulty encountered in attempts to acquire lattice images of the (010) face can be explained by the molecular packing on this surface compared with the more stable (001) surface. The exposed (010) surface is highly corrugated, terminated with rows of the cyanometallate ion or rows of the bis(amidinium) ion with the bis(amidinium) N-H groups protruding from the surface. The (001) surface is much less corrugated, with the hydrocarbon-rich ends of the bis(amidinium) ions protruding from the surface (Figure 10). A strong in-plane hydrogen-bonding network, characterized by cyano-water-cyano bridges along [100] and cyano-amidinium-cyano bridges along [010], stabilizes the (001) layers, whereas, only water-water bridges span the (001) lamellae along [001]. These structural features suggest that the surface energy of (001) is less than that of (010), which is consistent with our observation that the (001) faces typically are larger than the (010) faces. This may also explain the greater stability of the (001) surfaces during AFM image acquisition compared with (010).

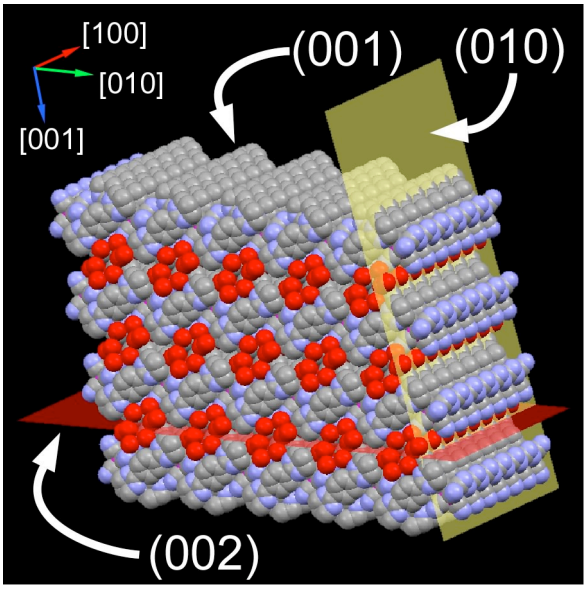

Figure 10. Space-filling representation of the molecular packing in **1-Fe** and **1-Ru**. The crystallographic faces labeled (001) and (010) are the primary faces traversing the long axis of the crystal, [100]. The red plane is positioned at the ½ position of the unit cell in the [001] direction and is labeled (002). This plane represents the location of a hydration layer comprising only water and separates lamellae of in-plane hydrogen-bonded bis(amidinium) cations and cyanometallate anions. The (001) face is characterized by a high density of nonpolar hydrocarbon ends of the bis(amidinium) molecules and prevents strong association with an aqueous medium. The (010) face (yellow plane) is populated by the cyano functional groups of the cyanometallate anions and is capable of hydrogen bonding with an aqueous medium. The (010) face is also strongly interdigitated and does not provide an obvious truncation surface on this face and may contribute to a roughened or corrugated topography.

A thermodynamic argument can be constructed to support the hypothesis that the (010) plane exists in a roughened (or less stable) configuration in comparison to the (001) plane by surmising the relative surface energies of these two planes in a slightly supersaturated aqueous solution. It is well known that for a given level of supersaturation, the roughness can be correlated to the calculated surface free energy of a particular crystal face. The surfaces of real crystal faces are heterogeneous at the scale of the molecular growth unit whereby the molecular constituents occupy sites on terraces, ledges, and kinks, each having a unique number of nearest neighbors in decreasing order, respectively.[33] The amount of energy required to remove a molecule from the crystal surface, ε_j, is proportional to the number of its nearest neighbors, N_j, and will have a specific bond enthalpy relating to its site configuration on the surface, where ΔH_f represents the enthalpy of formation in the bulk configuration, N_B is the number of nearest neighbors in the bulk configuration, and α_1 represents an arbitrary scale factor to compensate for crystal bond anisotropy and interfacial solvation effects associated with a particular face (eq. 1).

$$\varepsilon_j = \frac{\alpha_1 \cdot \Delta H_f}{N_A}\left(\frac{N_j}{N_B}\right) \qquad (1)$$

For a given growth unit, $N_{terrace} > N_{ledge} > N_{kink}$ and consequently $\varepsilon_{terrace} > \varepsilon_{ledge} > \varepsilon_{kink}$. The formation of terrace, ledge, and kink sites increases the configuration entropy (in that order) but with an enthalpic penalty (in the same order). The minimum free energy of the crystal surface represents the balance between these two factors, as described by eq. 2, in which the free energy, ΔG , is the sum of the enthalpic penalty associated with the removal of each molecule on the surface occupying a unique configurational state and the accompanying configurational entropy.

$$\Delta G = \sum_{ij} n_i \varepsilon_j - \alpha_2 kT \ln\left(\frac{W}{W_0}\right) \qquad (2)$$

The parameter W represents the combinatorial number of ways molecules (n_i) can occupy sites with bonding energies (ε_j), W_0 represents the sum of all molecules (n) having the same ε_0 , where $N_j = N_B/2$ (a molecularly flat plane populated by identical constituents having a half-bonded bulk configuration), α_2 represents a scale factor to compensate for effects such as crystal bond anisotropy and interfacial solvation, T is the temperature of the system, and k is Boltzmann's constant.

Because the molecular constituents of the (010) face are highly interdigitated and are decorated by cyano functional groups capable of charge-assisted hydrogen bonding with water molecules in the aqueous medium, the enthalpic penalty, ε , for dissociation of molecules attached to the (010) surface would be small due to strong solvation of these ions. Consequently, the configurational entropy would dominate on the (010) surface, supporting a higher density of ledges and kinks and a more dynamic crystal surface prone to dissolution and recrystallization at equilibrium conditions. This tendency may explain the failure to acquire lattice images on the (010) face. Such behavior also may produce a thick intermixing zone during heterocrystal formation because of repetitive dissolution/redeposition of the core and shroud compounds.

Concluding remarks

In situ AFM has revealed that under near-equilibrium conditions the isomorphous compounds **1-Fe** and **1-Ru** form perfectly aligned epitaxial (001) interfaces, whereas the dynamics of the (010) face preclude assignment of epitaxy. The roughness of the epitaxial interface between core and shroud compounds in heterocrystals of these compounds depends on the protocols used between growth of the core crystal and

its subsequent exposure to solutions of the shroud compound. Under conditions wherein the core crystal interface is stabilized the crystal surface tends to remain flat, creating conditions wherein the thickness of the compositional boundary defined by the two compounds is minimized. In contrast, under conditions wherein substantial roughening of the core surface occurs prior to deposition of the shroud compound the intermixing zone will likely achieve a thickness comparable to the roughness. Alternatively, the instability of the (010) surface can lead to repetitive cycles of dissolution and deposition of the core and shroud material, which also could produce a thick intermixing zone over time. Further EDS characterization using *indexed* heterocrystals to measure the thickness of the intermixing zones across the (001) and (010) interfaces will further elucidate the key parameters that regulate the definition of the growth boundary between the two isomorphous compounds.

Experimental

Materials and Crystal Growth. Potassium hexacyanoferrate(II) trihydrate (Sigma-Aldrich), potassium hexacyanoruthenate(II) trihydrate (Sigma-Aldrich), and a tosylated 1,4-bis(amidinium)benzene salt (synthesized) were used as obtained without further purification. All solutions were prepared using deionized water (18 MΩ) purified with a Barnstead E-Pure purification system. Preparation of crystals of **1-Fe** and **1-Ru** were synthesized by combining an aqueous solution of 0.02 M tosylated 1,4-bis(amidinium)benzene salt with an aqueous solution of 0.01 M potassium hexacyanoferrate(II) trihydrate salt for **1-Fe** crystals and an aqueous solution of 0.01 M potassium hexacyanoruthenate(II) trihydrate salt for **1-Ru** crystals. 500 mL aliquots of the mixed solutions were placed in a 1 mL glass vial and and left undisturbed at room temperature for two days. Crystals ranging in size from approximately 2 mm to 50 μm were removed from the glass vial with micromanipulation tools and were carefully dried under a gentle nitrogen stream. The selection of crystals presenting well-defined faces was obtained with a Leitz ERGOLUX optical compound microscope.

AFM Characterization. Crystals harvested by the methods described above were transferred to an AFM specimen disk that had been coated with partially cured (approximately 2 hours under a Blak-Ray B100 bulb at a distance of 6 inches) UV-curable thiolene adhesive (NOA-81, Norland Products, Inc.). After surplus particles on the disk were removed using a gentle nitrogen gas stream, the optical cement was completely cured by exposing the specimen to UV radiation for another 30 min. AFM was performed under ambient conditions (approximately 298 K) in air by contact mode using a Nanoscope IIIa Multimode system (Digital Instruments), a standard air tip holder, an E-scanner (Digital Instruments) with a maximum x-y scan range of 15 μm, and a 200 μm Si_3N_4 cantilever tip with a force constant of approximately 0.12 N/m. *In situ* AFM was performed in liquid by contact mode using a Nanoscope IIIa

Multimode system (Digital Instruments), a quartz glass liquid cell, an E-scanner (Digital Instruments) with a maximum x-y scan range of 15 μm, and a 200 μm Si_3N_4 cantilever tip with a force constant of approximately 0.12 N/m. All data were acquired in dual deflection and height modes with the driving gains optimized for the height channel such that deflection images were acquired as the derivative image or the error signal image of the height mode at a variety of scan rates chosen to optimize the tracking of the cantilever tip across the crystal surface. Typical scan areas were between 2 μm x 2 μm and 15 μm x 15 μm with the exception of the scan sizes for acquiring lattice images. Lattice image scan areas were between 8 nm x 8 nm and 50 nm x 50 nm.

Liquid media for *In situ* AFM was deionized water for dissolution investigations and a crystal growth solution comprising 0.005 M cyanometallate anion and 0.01 M bis(amidinium) cation for growth investigations. The solution was prepared and contained in a reservoir attached to the liquid cell with silicone tubing. Flow was controlled by a simple gravity-feed configuration from the solution reservoir such that the flow rate was approximately 0.5 mL/min. Exit flow was collected in a secondary reservoir also connected to the liquid cell with silicone tubing. For the acquisition of lattice images, the liquid cell was employed without an O-ring and 1 mL of deionized water was placed on the specimen disk with a syringe. This arrangement was preferential for the acquisition of lattice images because by not incorporating the tubing that is generally connected to the liquid cell, the motion of the piezo scanner was not impinged by tubing and the mass of the AFM head was reduced. These factors collectively improve the sensitivity of the piezo scanner to the crystal surface, which is necessary for acquiring well-defined lattice images. In addition to employing this configuration, incorporating only small volumes (1 mL) of growth solution around the crystal by allowing the solution droplet to 'pin' on the hydrophobic surface of the adhesive allowed growth equilibrium to be more easily attained and resulted in the creation of flatter, more stable crystal surfaces. The 1 mL solution reached saturation after 20 minutes and lattice images were collected using scan rates between 20 Hz and 120 Hz.

X-ray Diffraction. A unit cell of **1-Fe** was collected for a typical AFM crystal specimen using a Bruker Apex II single crystal diffractometer equipped with a Mo, $K\alpha_{II}$ (λ =0.7107 Å) monochromator. Unit cell data was superimposed over a series of video images to index the crystal and positively assign the [100] direction to the long axis of the crystal.

Acknowledgment

The authors gratefully acknowledge the support of the National Science Foundation (GOALI) and the *Molecular Design Institute* of New York University. The authors also acknowledge the Université de Strasbourg, Institut Universitaire de France, CNRS, and the Ministry of Education for financial support

and a scholarship to P.D. The authors also are grateful for the assistance of Dr. Samuel M. Hawxwell with X-ray crystallographic analysis.

Supporting Information Available. Raw AFM images corresponding to Figure 6.

References

[1] Chu, T. L.; Smeltzer, R. K. *J. Vac. Sci. Technol.* **1973**, *10*, 1-10.

[2] Herman, M. A.; Andersson, T. G. *Appl. Phys. A: Solids and Surf.* **1986**, *A41*, 243-52.

[3] Whitaker, T.; Martin, T. *Chemical Beam Epitaxy and Related Techniques*, **1997**, 299-329.

[4] Campbell, S. A. *Materials Science & Engineering, R: Reports*, **1997**, *R20*, 1-36

[5] Kuech, T. F.; Tischler, M. A. *Handbook of Semiconductor Technology* **2000**, *2*, 111-176.

[6] Swalen, J. D. *Ann Rev. Mater. Sci.* **1991**, *21*, 373-408.

[7] Forrest, S.R. *Chem. Rev.* **1997**, *97*, 1793-1896.

[8] Hooks, D.; Fritz T.; Ward M. D. *Adv. Mater.* **2001**, *13*, 227-241.

[9] Mitchell, C.; Yu, L.; Ward, M. D. *J. Am. Chem. Soc*. **2001**, *123*, 10830-10839.

[10] Carter, P. W.; Ward, M. D. *J. Amer. Chem. Soc.* **1993**, *115*, 11521-11535.

[11] Hooks, D.; Fritz, T.; Ward, M. D. *Adv. Mater.* **2001**, *13*, 227-241.

[12] Bonafede, S.; Ward, M. D. *J. Am. Chem. Soc.* **1995**, *117*, 7853-7861.

[13] Strohmaier, R.; Ludwig, C; Petersen, J.; Gompf, B.; Eisenmenger, W. *Surf. Sci.* **1994**, *318*, L1181-L1185.

[14] MacDonald, J. C.; Dorrestein, P. C.; Pilley, M. M.; Foote, M. M.; Lundburg, J. L.; Henning, R. W.; Schultz A. J.; Manson, J. L. *J. Am. Chem. Soc.* **2000**, *122*, 11692

[15] Noveron, J.C.; Lah, M. S.; Del Sesto, R. E.; Arif, A. M.; Miller J. S.; Stang, P. J. *J. Am. Chem. Soc.* **2002**, *124*, 6613.

[16] Luo, T.-J. M.; MacDonald J. C.; Palmore, G. T. R. *Chem. Mater.* **2004**, *16*, 4916.

[17] (a) Catala, L.; Brinzei, D. ; Prado,Y.; Gloter, A.; Stéphan, O.; Rogez, G.; Mallah T. *Angew. Chem. Int. Ed.* **2009**, *48*, 183-187. (b) Furukawa, S.; Hirai, K.; Nakagawa, K.; Takashima, Y.; Matsuda, R.; Tsuruoka, T.; Kondo, M.; Haruki, R.; Tanaka, D.; Sakamoto, H.; Shimomura, S.; Sakata, O.; Kitagawa S. *Angew. Chem. Int. Ed.* **2008**, *47*, 1-6.

[18] Ferlay, S.; Hosseini, M. W. *Chem. Commun*. **2004**, 788-789.

[19] Dechambenoit, P.; Ferlay, S.; Hosseini, M. W. *Cryst. Growth Des.* **2005**, *5*, 2310-2312.

[20] Brès, E. F.; Ferlay, S.; Dechambenoit, P.; Leroux, H.; Hosseini M. W. *J. Mater. Chem.* **2007**, *17*, 1559-1562.

[21] (a) Ward, M. D. *Chem. Rev.* **2001**, *101*, 1697-1725. (b) Carter, P. W.; Hillier, A. C.; Ward, M. W. *J. Am. Chem. Soc.* **1994**, *116*, 944-953. (c) Jung, T.; Sheng, X.; Choi, C H.; Kim, W-S.; Wesson, J. A.;

Ward, M. D. *Langmuir* **2004**, *20*, 8587-8596. (d) Ng J D; Kuznetsov Y G; Malkin A J; Keith G; Giege R; McPherson A. *Nucl. Acids Res*. **1997**, *25*, 2582-8. (e) De Yoreo, J. J.; Qiu, S. R.; Hoyer J. R. *Am. J. Physiol*. **2006**, *291*, F1123-31. (f) Kepler, K. D.; Gewirth, A. A. *Surface Science*, **1994**, *303*, 101-13. (g) Uosaki, K.; Koinuma, M. *Solar Energy Mater. Solar Cells* **1995**, *38*, 347-8. (h) Harron, H. R.; Pritchard, R. G.; Cope, B. C.; Goddard, D. T. *Internat. J. Electronics* **1996**, *81*, 485-489. (i) Land, T. A.; De Yoreo, J. J.; Lee, J. D. *Surf. Sci*. **1997**, *384*, 136-155. (j) Shindo, H.; Ohashi, M. *Appl. Phys. A: Mater. Sci. Proc*. **1998**, *66*, S487-S490. (k) Reyhani, M. M.; Freij, S.; Parkinson, G. M. *J. Cryst. Growth* **1999**, *198/199*, 258-263. (l) Mauri, A.; Moret, M. *J. Cryst. Growth* **2000**, *208*, 599-614. (m) Kitamura, M.; Onuma, K. *J. Coll. Interface Sci*. **2000**, *224*, 311-316. (m) De Yoreo, J. J.; Orme, C. A.; Land, T. A. *Adv. in Crystal Growth Res*. **2001**, 361-380. (n) Plomp, M.; McPherson, A.; Malkin, A. J. *J. Cryst. Growth* **2002**, *237-239*, 306-311. (o) Beekmans, L. G. M.; Vallee, R.; Vancso, G. J. *Macromolecules* **2002**, *35*, 9383-9390. (p) Petrova, E. V.; Gvozdev, N. V.; Rashkovich, L. N. *J. Optoelectron. Adv. Mater*. **2004**, *6*, 261-268. (q) Ito, A.; Yamanobe-Hada, M.; Shindo, H. *J. Cryst. Growth* **2005**, *275*, e1691-e1695.

[22] Bosshard, C.; Sutter, K.; Prêtre, P.; Hulliger, J.; Flörscheimer, M.; Kaatz, P.; Günter, P. *Organic Nonlinear Optical Materials (Advances in Nonlinear Optics, Vol 1)*. Gordon and Breach Science Publishers, Postfach, Switzerland, **1995**.

[23] Aakeröy, C. B.; Beatty, A. M. *CrystEngComm*, **1998**, *1*, 39-49.

[24] Fraxedas, J. *Adv. Mater.* **2002**, *14*, 1603-1614.

[25] (a) Vegard, L. *Z. Phys*. **1927**, *43*, 299-308. (b) Vegard, L.; Dale, Hjalmar. *Z. Kristall, Kristallgeom., Kristallphy., Kristallchem.* **1928**, *67*, 148-161.

[26] (a) Ward, M. D.; Calabrese, J. C. *Organometallics* **1989**, 8, 593. (b) M. D. Ward, *Organometallics*, **1987**, *6*, 754.

[27] Liu, X-Y.; Arkenbout, G.; Bennema, P.; van Hoof, P. *J. Cryst. Growth* **1993**, *133*, 322-328.

[28] Vlachos, D. G.; Schmidt, L. D.; Aris, R. *Phys. Rev. B*. **1993**, *47*, 4896-4909.

[29] Adamson, A. W. *Physical Chemistry of Surfaces, Sixth Edition.* Wiley, New York, N. Y., **1997.**

[30] Israelachvili, J. N. *Intermolecular and Surface Forces, Second Edition.* Acedemic Press, London, **1991**.

[31] Miller, C. A.; Neogi, P. *Interfacial Phenomena: Equilibrium and Dynamic Effects*. Marcel Dekker, New York, N.Y., **1985**.

[32] Hiemenz, P. C.; Rajagopalan, R. *Principles of Colloid and Surface Chemistry, Third Edition.* Marcel Dekker, New York, N.Y., **1997**.

[33] Tiller, W. A.; *The Science of Crystallization; Microscopic Interfacial Phenomena*. Cambridge University Press, New York, N.Y., **1991**.